Research Article | Vol. 28, No. 8 / 13 April 2020 / Optics Express 10981
Optics EXPRESS

Influence of temporal averaging in the performance of a rotating retarder imaging Stokes polarimeter

ÁNGEL LIZANA,[1,4] JUAN CAMPOS,[1] ALBERT VAN EECKHOUT,[1,5] AND ANDRÉS MÁRQUEZ[2,3]

[1]Departamento de Física, Universitat Autònoma de Barcelona, Bellaterra, 08193, Spain
[2]Dept. de Física, Ing. de Sistemas y Teoría de la Señal, U. de Alicante, Ap. 99, Alicante, 03080, Spain
[3]I.U. Física Aplicada a las Ciencias y las Tecnologías, U. de Alicante, Ap. 99, Alicante 03080, Spain
[4]angel.lizana@uab.es
[5]albert.vaneeckhout@uab.cat

Abstract: We study the optimum operating conditions for a rotating retarder fixed polarizer (RRFP) when the measurements are not quasi-instantaneous but time-averaged. We obtain the optimum retardance and retarder orientations as a function of the integrated angle interval. We also study how the increase in the number of time-averaged measurements leads to a better equally weighted variance (EWV) value, and thus, to a better performance of the polarimeter in terms of noise amplification for the case of additive noise. Two different analyzers configurations are studied in this work: uniformly spaced retarder angles and when measurements are taken at optimum angles (non-uniformly spaced angles). We also consider the case of polychromatic illumination. We discuss the best measurement conditions in terms of the signal-to-noise ratio depending on whether there is a fixed or a limited amount of photons per measurement.

1. Introduction

Acquisition of polarimetric information is becoming more and more important since there is an increasing number of applications where this information finds practical use. Such applications are for example biomedical physics [1–3], astronomy [4,5], polarizing sample characterization [6–8], among others. In point polarimeters we are interested in the analysis of the state of polarization (SOP) at a single point of the light beam, which can be done with very high time resolutions [9]. When polarimetric images are necessary, image polarimeters are required. These image polarimeters calculate the Stokes vector for each pixel of the image, so they are based on more complex architectures and data processing. Imaging polarimeters can be categorized [10], as division of time polarimeters (DoTP), amplitude (DoAmP), aperture (DoAP), and focal-plane (DoFP).

One of the well-known and classical polarimeter architectures used is the rotating retarder fixed polarizer (RRFP) Stokes polarimeter [11,12], applied both in point and in imaging polarimeters. RRFP belong to the category of DoTPs, where measurements are acquired sequentially in time. In any polarimeter, the minimum amount of intensity measurements required to obtain a full characterization of the SOP is four. In the case of the RRFP this means that for a particular fixed retardance value of the retarder, four intensity measurements need to be taken at four different orientations of the neutral lines of the retarder with respect to the transmission axis of the polarizer. At each of these orientations the polarimeter is setting a different polarization analyzer. Sabatke et al. [11] obtained that the optimum retardance of the waveplate, in terms of noise minimization, is 132°. The figure of merit used for this assessment is the equally weighted variance (EWV) [11,12]. They also analyzed how the EWV decreases as the number of different analyzers considered for the intensity measurements increase. In their analysis, for each

#385623 https://doi.org/10.1364/OE.385623
Journal © 2020 Received 10 Dec 2019; revised 5 Feb 2020; accepted 5 Feb 2020; published 31 Mar 2020

Optics EXPRESS

polarization analyzer considered, the corresponding angle between the retarder and the polarizer remains constant during the measurement time. This means that the analyzer is fully polarized.

However, depending on the experimental configuration of the rotating polarimeter used, this fully-polarized analyzers scenario is not always ensured. For instance, if the polarization analyzer is a consequence of a time-integration along a certain retarder orientation range (which results in a quite common scenario in experimental systems depending on the synchronization between the detector acquisition time and the retarder rotation), the resulting integrated analyzer vector is partially polarized. In the case of point polarimeters, it is possible to obtain quasi-instantaneous measurements since integration time in detectors can be very small. However, in imaging polarimeters the integration time is limited by the integration time of the camera, which is larger than for detectors.

In the present paper we study the optimum operating conditions for a RRFP when the measurements are not quasi-instantaneous. Under such scenario, we obtain the optimum retardance as a function of the integration time and we compare this result with a common experimental configuration, the case when a quarter waveplate is used as retarder in RRFPs. We also study how the increase in the number of measurements leads to a better EWV value, and thus, to a better performance of the polarimeter in terms of noise amplification. Depending on the criterion used to select the different retarder orientations to construct the RRFP analyzer basis, two different analyzers configurations are studied in this work. First, measurements are obtained at uniformly spaced angles along half retarder rotation. Second, we also analyze the situation when measurements are taken at optimum angles (non-uniformly spaced angles).

There are applications, such as in tissue structural analysis [3,13–16], where various illumination wavelengths are used. If a conventional non-achromatic retarder is applied, the effective retarder retardance changes with the applied wavelength. This situation is also evaluated in this paper, to find the optimal working conditions for multi-wavelength polarimetric imaging. Finally, something we also have to consider is the effect of the integration time and number of measurements on the signal-to-noise ratio of the measured Stokes vector. We will consider the usual situation where additive noise sources are predominant. We discuss the best measurement conditions depending if there is a fix or a limited amount of photons per measurement. In other words, the signal-to-noise ratio (SNR) relationship with the integration time is also considered in this manuscript.

2. Theory for a RRFP with non-instantaneous intensity measurements

2.1. RRFP optical scheme: generation of polarization analyzers and their dependence with time integration

In Fig. 1 we show the general scheme for a RRFP. We consider a rotating linear retarder with a retardance φ, with the transmission axis for the linear polarizer (linear analyzer) set along the X-axis (which in Fig. 1 represents the laboratory vertical), and where $\theta(t)$ is the angle of the fast axis of the retarder with respect to the X-axis. The intensity detected as a function of the retardance φ, the orientation of the linear retarder $\theta(t)$, and the incident SOP is given by:

$$\begin{aligned} I(\varphi,\theta(t);\vec{S}_{in}) = \vec{A}^T\vec{S} = \frac{1}{2}\{S_0 + (\cos^2(2\theta(t)) + \cos(\varphi)\sin^2(2\theta(t)))S_1 \\ + (1-\cos(\varphi))\cos(2\theta(t))\sin(2\theta(t))S_2 - \sin(\varphi)\sin(2\theta(t))S_3\}, \end{aligned} \tag{1}$$

where $\vec{A}^T$ is the transposed (T) Stokes analyzer in which the state of polarization (SOP) of the input beam, described by the Stokes vector $\vec{S}$, is projected. The Stokes vector $\vec{S}$ consists of four real components (S_0, S_1, S_2, S_3). To obtain the integrated time-averaged expression is more

Optics EXPRESS

convenient to express the previous equation without the powers in the trigonometric functions:

$$I(\varphi,\theta(t);\vec{S}) = \vec{A}^T\vec{S} = \frac{1}{2}\left\{S_0 + \left(\frac{\cos(\varphi)+1-(\cos(\varphi)-1)\cos(4\theta(t))}{2}\right)S_1 + (1-\cos(\varphi))\frac{\sin(4\theta(t))}{2}S_2 - \sin(\varphi)\sin(2\theta(t))S_3\right\}. \tag{2}$$

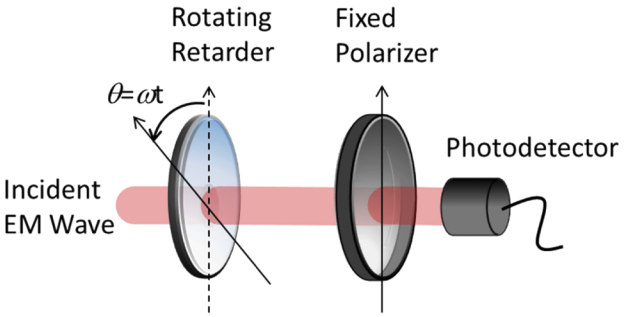

Fig. 1. Diagram for the rotating retarder fixed polarizer (RRFP) Stokes polarimeter.

This expression can be interpreted as the projection of the input SOP onto the Stokes analyzers set by the optical configuration shown in Fig. 1. By considering the Mueller matrices of a linear retarder, of retardance φ and orientation $\theta(t)$ [17], and a linear polarizer oriented in the X-axis direction, these Stokes analyzers can be written as,

$$\vec{A}(\varphi,\theta(t)) = \frac{1}{2}\begin{pmatrix} 1 \\ \frac{\cos(\varphi)+1-(\cos(\varphi)-1)\cos(4\theta(t))}{2} \\ (1-\cos(\varphi))\frac{\sin(4\theta(t))}{2} \\ -\sin(\varphi)\sin(2\theta(t)) \end{pmatrix}. \tag{3}$$

When we consider the integration time of the detection camera, the detected intensity corresponds to the integrated value across an angle interval $\Delta\theta$ around the central value $\bar{\theta}$. The trigonometric expressions averaged across an angle interval $\Delta\theta$ are given by:

$$\langle\cos(m\theta)\rangle_{\Delta\theta} = \mathrm{sinc}(m\Delta\theta/2)\cos(m\bar{\theta}) \tag{4}$$

$$\langle\sin(m\theta)\rangle_{\Delta\theta} = sinc(m\Delta\theta/2)\sin(m\bar{\theta}) \tag{5}$$

where m is a multiplicative factor number and the *sinc* and $<\mathrm{f}(\theta)>_{\Delta\theta}$ function are defined as,

$$\mathrm{sinc}(\alpha) \equiv \sin\alpha/\alpha \tag{6a}$$

$$\langle f(\theta)\rangle_{\Delta\theta} = \frac{1}{\Delta\theta}\int_{\bar{\theta}-\Delta\theta/2}^{\bar{\theta}+\Delta\theta/2} f(\theta)d\theta. \tag{6b}$$

As a result, the amplitudes of the cosine and sine, Eqs. (4) and (5), are modulated by the *sinc* function with $\Delta\theta/2$ as argument: the larger the angle interval $\Delta\theta$, the smaller the *sinc* value.

Optics EXPRESS

Taking into account relations given in Eqs. (4) and (5), the analyzers in Eq. (3) can be angular-averaged as:

$$\left\langle \vec{A}(\varphi,\theta(t))\right\rangle_{\Delta\theta} = \frac{1}{2}\begin{pmatrix} 1 \\ 0.5(\cos(\varphi)+1) - 0.5(\cos(\varphi)-1)\cos(4\bar{\theta})\mathrm{sinc}(2\Delta\theta) \\ 0.5(1-\cos(\varphi))\sin(4\bar{\theta})\mathrm{sinc}(2\Delta\theta) \\ -\sin(\varphi)\sin(2\bar{\theta})\mathrm{sinc}(\Delta\theta) \end{pmatrix}. \tag{7}$$

Due to the time average over the angle interval $\Delta\theta$, the analyzers in Eq. (7) could result in partial polarized measurement vectors. Under this scenario, we are interested in calculating the degree of polarization (DOP) for the analyzers expressed in Eq. (7). In Fig. 2 we plot the dependence of the DOP with the integrated angle interval $\Delta\theta$. We show the curves for two particular retardance values and two orientations of the linear retarder. The values considered for the retardance are within the optimized results that we will show in the next Sections. We have considered the orientations θ at 0° and 45°, which provide the curves with maximum and minimum DOP for any given retardance: we note that the curves repeat with a periodicity of 90° in the orientation θ. We see that for the four curves the DOP decreases with $\Delta\theta$, starting as full polarized light at $\Delta\theta = 0$ and diminishing to values in the range 0.8 at $\Delta\theta = 0$. Therefore, we confirm that the analyzer vectors available by using time integrated RRFP polarimeters are significantly partially polarized.

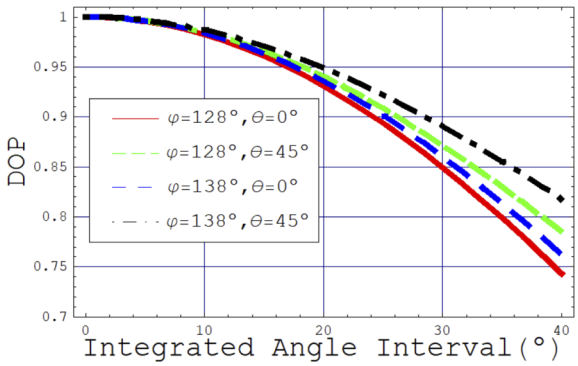

Fig. 2. Dependence of the DOP with $\Delta\theta$ for the angle averaged analyzers in the RRFP.

2.2. *RRFP measuring principle. Effects of temporal integration and noise sources*

To obtain the values for the four components of $\vec{S}$, i.e. to completely characterize the input polarization, a minimum of four independent intensity measurements are necessary, i.e. at four different mean orientations $\bar{\theta}$. Since measurements are taken while the retarder is rotating, the intensity measurements correspond to the value for a certain integrated angle interval $\Delta\theta$. We note that any polarization analyzer set by the RRFP polarimeter is repeated with a periodicity of half a rotation, and thus, in order to analyze at which angular positions the measurements are taken we limit our attention to the angle interval 0 to 180 degrees. In the analysis we also need to consider that the integration interval $\Delta\theta$ must be equal or smaller than the angular separation between consecutive orientations $\bar{\theta}$ to avoid overlap.

The resultant intensity values on the sensor pixels are given by,

$$\vec{I} = W\vec{S}, \tag{8}$$

where W is the $N\times 4$ measurement matrix whose rows are given by the N analyzers, $\vec{S}$ is the 4×1 column vector for the incident SOP under measurement, and the resulting N intensity values are

Optics EXPRESS

arranged as column vector $\vec{I}$. When matrix W has been calibrated, inversion of Eq. (8) provides the incident SOP as a function of the intensities measured at the selected analyzer orientations [17,19]. In general matrix W is not square and the pseudoinverse estimator is used,

$$\vec{S} = W^{+}\vec{I} \tag{9}$$

where

$$W^{+} = (W^{T}W)^{-1}W^{T} \tag{10}$$

Matrix inversion amplifies the noise associated with the intensity measurements. This can be minimized by selecting N polarization analyzers producing a matrix W as far as possible of singular matrices. A typical figure of merit to evaluate the adequacy of W is the condition number (CN) [20]: the lower its value the better conditioned the matrix is, with a minimum theoretical value of $CN_{min} = \sqrt{3} = 1.7321$ for polarimetric systems [10]. Since CN does not take into account redundant measurements (N > 4), it is more appropriate to use the equally weighted variance (EWV) figure of merit when more than four polarization analyzers are considered [11,12,21,22]. For the definition of EWV first let us note that the variance v_j in the jth component of the estimated Stokes vector is [11],

$$v_j = \sum_{k=0}^{N-1} (W^{+}_{j,k})^2 u_k, \tag{11}$$

where u_k is the variance of the intensity noise in the kth analyzer. We note that Eq. (11) is valid for the general case of additive white Gaussian noise (AWGN) in the intensity measurements [11], which is the one we consider in the paper. To simplify, we consider the general approximation of equal variance in the intensity noise for all the analyzers, i.e. $u_k = u$ for all k. The usual definition of EWV is given by

$$EWV = \frac{\sum_{j=0}^{3} v_j}{u} = \sum_{j=0}^{3}\sum_{k=0}^{N-1} (W^{+}_{j,k})^2, \tag{12}$$

where EWV corresponds to the added variance for the 4 Stokes components divided by the intensity variance. With this definition, the EWV focuses on the noise amplification due to the set of analyzers composing the measurement matrix.

To model the detection process and the intensity noise sources we consider the European Machine Vision Association (EMVA) 1288 Standard [23] which details a standard set of models and procedures to characterize CMOS and CCD cameras and light sensors. The basic intensity noise sources in the detection process are the photon shot noise (PSN), the dark current noise and the read-out noise. The PSN is due to the discrete and random arrival of the photons onto the sensor, it is signal dependent and follows Poisson statistics. Even when no light is incident onto the sensor, there is still charge generation in the sensor, due to thermal effects, which produces the dark current. This dark current can be measured and subtracted from the signal. However, since it fluctuates, its effect cannot be completely eliminated and remains as the dark current noise. This is an additive noise which follows a Poisson distribution. It is signal independent and increases linearly with the time of exposure. The last source of intensity noise is also additive and signal independent, and it is the read-out noise. This is produced by the electronics, mainly by the on-chip amplifier, and adds a constant number of electrons per acquisition frame, that is, it does not depend on the exposure time. We note that both dark current noise and read-out noise are additive and they contribute even when no light is incident onto the sensor.

Depending on the application and on the camera characteristics, the main source of noise affecting the signal-to-noise ratio (SNR) is different. If there is not much light arriving onto the

Optics EXPRESS

sensor, normally additive sources are dominant, which can be modelled as AWGN. In the case of dark current noise, the variance is given by the average dark current $\langle I_{dark} \rangle$ multiplied by the integration time Δt

$$u_{dark} = \langle I_{dark} \rangle \, \Delta t. \tag{13}$$

The read-out noise variance u_{read} is a constant number of electrons per frame. We see that depending on the number of analyzers considered in the measurement system and on the magnitude of the intensity integration interval the intensity variance will be different, which will influence the estimated Stokes vector variance.

To have an estimation of the order of magnitude of the integration intervals and the number of available measurements, let us consider a camera with an acquisition frequency of 100 frames/s and where the retarder is rotating at 5 Hz (300 rpm), which is the value for the commercial PAX1000 polarimeters from Thorlabs [18] (of the RRFP kind). With these values, in half a rotation the camera is able to sequentially acquire 10 frames, i.e. 10 intensity images, each with a maximum integration time Δt_M of 10 ms or, what is equivalent, a maximum integration angle interval $\Delta\theta$ of 18°.

3. Results

In order to optimize the retardance and orientations in the RRFP, there are two typical figures of merit, CN and EWV. We have done the calculations by using both metrics and we have obtained very similar results. However, CN produces smoother variations as a function of the number of analyzers N, and it is the figure of merit that we have used in this work. Both CN and EWV follow a similar behavior in the sense that minimizing one of them produces the minimization of the other. Actually, as pointed out by Foreman and Goudail [22,24], the CN is proportional to the square root of the EWV. The RRFP can be operated according to different configurations. In the following we have chosen to show the optimized results in the situations of a major interest.

3.1. Uniformly spaced angles

Since the retarder is continuously rotating in the RRFP, an efficient way to operate the polarimeter is by acquiring various intensity images at uniformly spaced angles. In the plots in Figs. 3(a) and 3(b) we show the two dimensional contour plots for the CN and the EWV as a function of both the number of analyzers N and the integrated angle interval $\Delta\theta$. First thing we note is that in both cases the figures of merit degrade as $\Delta\theta$ increases. Second characteristic is that the CN is constant with N, whereas the EWV diminishes with the increase in N. We note that for N = 4 the RRFP does not produce a complete polarimeter as their values tend to infinity (this is why graphs in Fig. 3 start at the value N = 5). This situation is explained because uniformly spaced angles generate four polarization analyzers that, when represented in the Poincaré Sphere space, are restricted into a plane, and thus, they do not enclose a volume. Note that complete polarimeters require that their polarization analyzers, when represented over the Poincaré Sphere, enclose volumes different than zero [12].

In Figs. 4(a) and 4(b) we show respectively the CN and the EWV in a curve plot for a fixed N value [they are the values corresponding to a horizontal line in Figs. 3(a) and 3(b)], which provides easier evaluation of quantitative values. In Fig. 4(a), as discussed in Fig. 3(a), we see that the CN is the same whatever the number of analyzers N as all curves are superposed. Its minimum value is larger than the theoretical minimum of 1.7321 since the orientation angles are restricted to be uniformly spaced and the optimum distances between analyzers are not achieved. We note that even at such a large $\Delta\theta$ value of 40°, the CN is still very small. Most of polarimeters proposed in literature present CNs within the range [1.73-4], so CNs smaller than 3 can be considered in general as acceptable values, and provide performances suitable for most polarimetric applications [25]. In Fig. 4(b) the EWV decreases with N (different color curves)

Optics EXPRESS

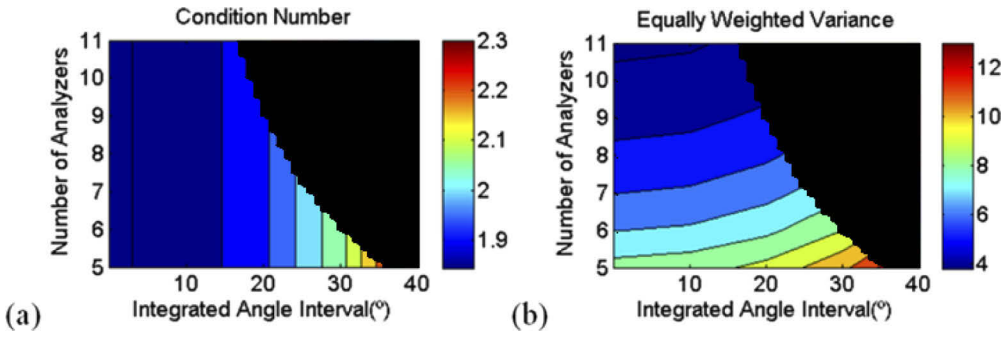

Fig. 3. Optimization results for the RRFP with uniformly spaced angles. (a) CN map, and (b) EWV map, obtained as a function of the number of analyzers N and the integrated angle interval $\Delta\theta$.

both when instantaneous measurements are taken, $\Delta\theta = 0$, or when $\Delta\theta$ has a finite value. Note that in previous papers [11], only the situation $\Delta\theta = 0$ was considered.

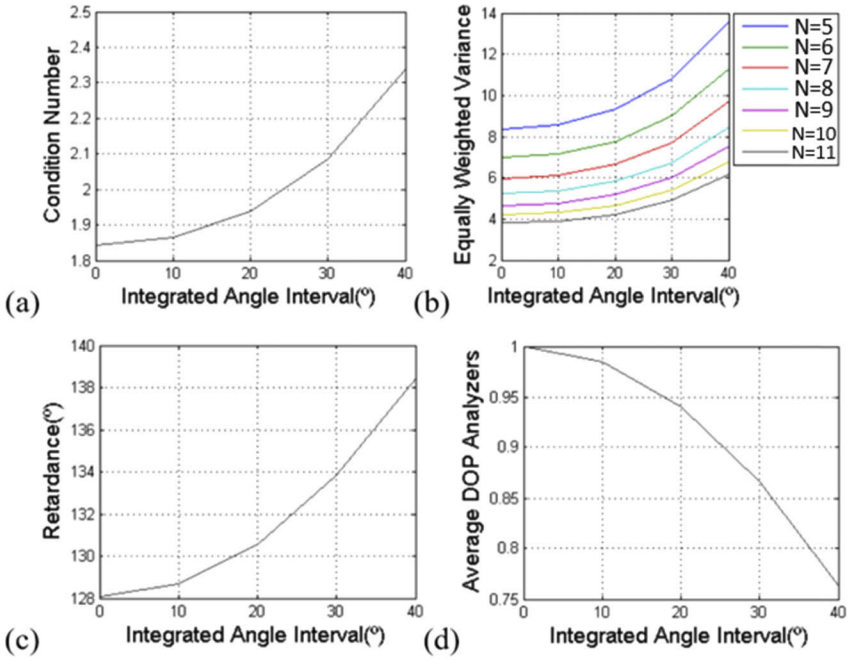

Fig. 4. Optimization results for the RRFP with uniformly spaced angles. (a) CN, (b) EWV, (c) Retardance, and (d) Average DOP of the analyzers.

We know that in general for polarimeters with purely polarized light analyzers, the EWV varies inversely with the number of analyzers N [22,26,27] both for AWGN and PSN. In the paper we are dealing with additive noise, in which case $EWV = 40/N$ [22,26,27]. We have used this a priori knowledge to propose a fitting power function whose coefficient varies polynomically with the integration angle interval $\Delta\theta$, and we have obtained the following result:

$$EWV(\Delta\theta, N) = \left(a + b\,\Delta\theta^2 + c\,\Delta\theta^4 + d\,\Delta\theta^6 + e\,\Delta\theta^8\right) \Big/ N, \tag{14}$$

Optics EXPRESS

where $\Delta\theta$ is in degrees, and with coefficients: a = 41.85, b = 0.01079, c = 2.417e-06, d = 4.152e-10, and e = 1.317e-13. We note that the fit is excellent since the coefficient of determination R^2 is equal to one and the root mean squared error (RMSE) between the values predicted by Eq. (14) and the data is 2.564e-9, which is a very low value. Polynomials with even powers provide the best results, with the best fit given by the indicated 8th degree polynomial: the RMSE for the 6th degree polynomial fit is still a low value, 0.0002423. From this 8th degree polynomial result, we see that for ideal instantaneous measurement ($\Delta\theta = 0$) the coefficient is 41.85 [a coefficient from Eq. (14)], slightly larger than 40 since the orientations of the retarder are restricted to be uniformly spaced.

To provide graphical proof of the goodness of the fitting polynomial in Eq. (14), in Fig. 5 we show the difference between the EWV calculated with the fitted expression and the EWV data points in Fig. 4(b). This difference is normalized by the value of each of the EWV data points and represented as a function of the integrated angle interval $\Delta\theta$. The different curves correspond to different number of measurement analyzers, indicated in the legend as in Fig. 4(b). We see that the fit is excellent, as said after Eq. (14): the normalized difference is smaller than ±1e-9, with larger values at the right end of the $\Delta\theta$ axis.

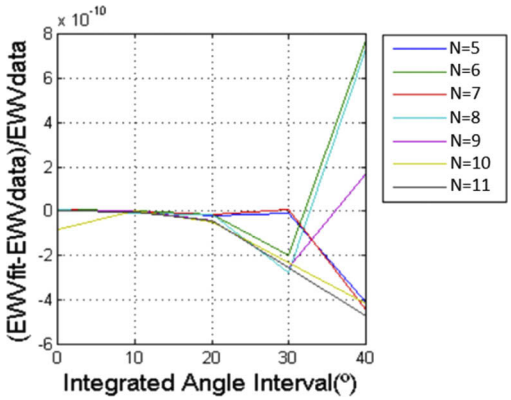

Fig. 5. Difference between the EWV calculated with the fitting polynomial [Eq. (14)] and the EWV data points, normalized by the data points.

In Figs. 4(c) and 4(d) we show respectively the optimum retardance (found by using the CN and EWV criteria) and the average DOP as a function of the integrated angle interval $\Delta\theta$. The average DOP is calculated by applying the relation $DOP = \sqrt{S_1^2 + S_2^2 + S_3^2}\,/\,S_0$ to each of the N analyzers whose Stokes vector is given by Eq. (7), and then averaging the DOP for the N analyzers. We see that in both cases the results do not depend on the number of analyzers as all colored curves are overlapped. In Fig. 4(c) we see that the optimum retardance varies with $\Delta\theta$ from 128° to 138.4°. This is interesting since the optimum retardance value in the paper by Sabatke et al. [11] is 132°, this retardance value was obtained for instantaneous intensity measurements, i.e., $\Delta\theta = 0$, and when the uniformly spaced restriction was not applied. Therefore, results in Fig. 4 constitute a generalization of the study provided in [11]. Going back to Fig. 4(c), in the range interval from $\Delta\theta = 0$ to $\Delta\theta = 40°$, the optimum retardance changes from 128° to 138.4°. In Fig. 4(d) the average DOP decreases monotonically with $\Delta\theta$. It is interesting to note that at such a large value as $\Delta\theta = 40$ the analyzer vectors are clearly partially polarized. However, the CN [Fig. 4(a)] still shows a very good value and the RRFP can be efficiently used as a polarimeter in terms of noise amplification. This is consistent with the previous analysis presented in Fig. 2 for the DOP of the averaged analyzer.

Optics EXPRESS

To get a deeper insight, in the following we provide a geometrical visualization of the results discussed above. In Figs. 6(a) and 6(b) we show the SOPs corresponding to the optimal analyzers basis represented onto the Poincaré sphere. We have chosen to conduct this representation for N = 5. We show the curves corresponding to different angular integration intervals and the dots correspond to the optimal analyzers. The outer curve corresponds to the case $\Delta\theta = 0$ and the inner curve is given by $\Delta\theta = 40$. We clearly see in Fig. 6(b) that by increasing the integration interval, the analyzers are no longer fully polarized SOPs, as they are not at the sphere surface but fall inside. In fact, when the integration angle interval increases, the volume of the inscribed geometrical figure, whose vertices are the optimal analyzers, decreases. This indicates that the uncertainty in the determination of a SOP under test increases [11,12].

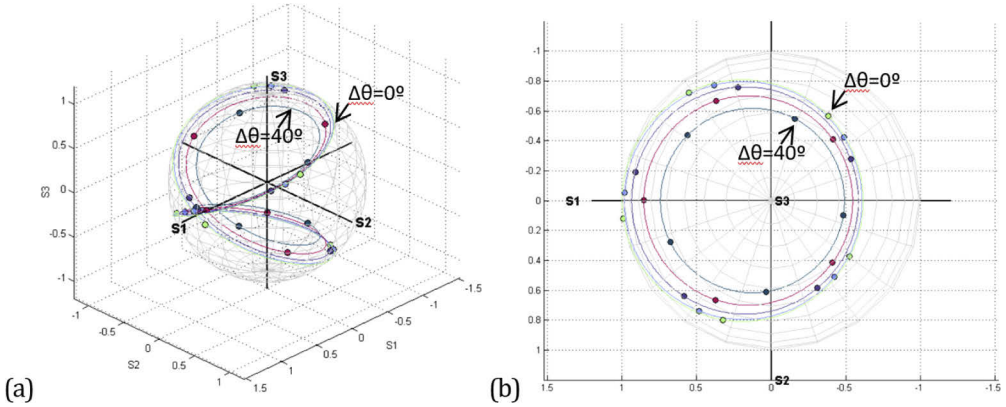

Fig. 6. Representation on the Poincaré sphere of the optimal analyzers for N = 5. The different trajectories are related with different integrated angle intervals: 0° (outer path), 10°, 20°, 30°, and 40° (inner path). In each of the trajectories the circles indicate the location of a particular set of measuring analyzers. (a) and (b) show different points of view of data in the Poincaré Sphere space.

In this Section we have been able to obtain an analytical expression for the EWV as a function of the number of polarization analyzers and the integration angle interval. This includes as a particular result the case for totally polarized analyzers, which is the usual case considered in the literature. This analytical expression for EWV is very useful since it can be used to evaluate the SNR under different kinds of noise sources as we will show in Section 4. We also find very important the results obtained for the optimum retardance of the waveplate in the RRFP and its variation with the integration angle interval.

3.2. *Unrestricted orientations*

It is interesting to evaluate what are the results if we remove the uniform angle interval restriction. This is not a practical situation since it means a non-periodic acquisition frame rate, but it is worth for academic purposes for the sake of comparison with the most general framework. In Figs. 7(a) and 7(b) we show the results for CN and EWV as a function of $\Delta\theta$. When compared with the equivalent results in Figs. 4(a) and 4(b), the values are slightly better, however very similar. Therefore, the uniformly-spaced angle (case analyzed in Section 3.1) is very close to the optimal situation reached without restrictions in the orientation and, taking into account its practicality, is recommended for RRFP implementations. We note that in Fig. 7(a) the curve for N = 5 has slightly larger values. This is consistent with the results presented by Foreman and Goudail [22,24], where they explain that in the context of optimal polarimetry, the case for N = 5 is the only exception for $N \geq 4$ where there is no distribution of the measurement

Optics EXPRESS

states over the Poincaré sphere satisfying a spherical 2 design. They find [22] that for N = 5 the minimum achievable values for CN and EWV are slightly larger than the tendency exhibited by the other N cases where the optimal measurement states form a spherical 2 design. A spherical 2 design is defined as a collection of N points on the surface of the unit sphere, i.e. in our case the measurement states over the Poincaré sphere, for which the normalized integral of any polynomial function of degree 2 or less is equal to the average taken over the N points [22,24]. In Fig. 7(c) we show the optimal retardance as a function of $\Delta\theta$. The values are slightly higher than in Fig. 4(c). Now we obtain the well-known result of 132° of optimal retardance for $\Delta\theta = 0$ as given by Sabatke et al. [11]. We also see that the curve for N = 5 has a different behavior with a discontinuity between the $\Delta\theta$ angles 28.5° and 29°. The values for the average DOP in Fig. 7(d) are quite similar to the ones obtained in Fig. 4(d).

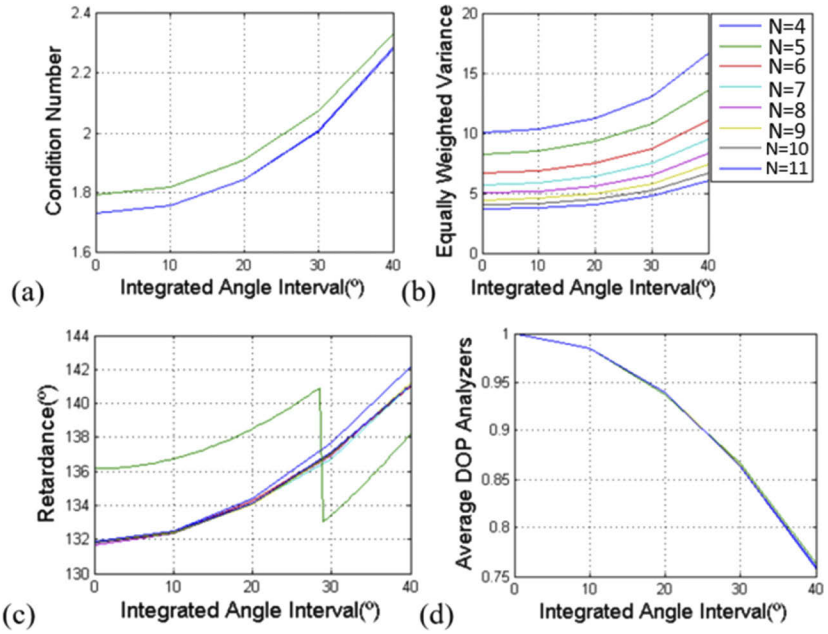

Fig. 7. Optimization results for the RRFP with unrestricted orientations. (a) CN, (b) EWV, (c) Retardance, and (d) Average DOP of the analyzers.

As we did in Section 3.1, we have fitted the results for the EWV as a function of the integration angle interval and the number of analyzers. We have taken out the data for N = 5 since they do not follow the pattern of most data in Fig. 7, and we have obtained the following fitting expression,

$$EWV(\Delta\theta, N) = \left(a' + b'\,\Delta\theta^2 + c'\,\Delta\theta^4 + d'\,\Delta\theta^6\right) \Big/ N, \tag{15}$$

where $\Delta\theta$ is in degrees, and with coefficients: a'=40, b'=0.01104, c'=2.202e-06, and d' = 7.977e-10. Once again the fit has the coefficient of determination R^2 equal to one. The RMSE value is 0.01121, still a good value even though not that low as it happened in Eq. (14). In the present case, the 8th degree polynomial fit does not decrease significantly the RMSE value, thus we consider the 6th degree polynomial as the best fit. We will show in Fig. 8 a graphical proof of the goodness of the fit. We see that for ideal instantaneous measurement ($\Delta\theta = 0$) the coefficient is 40 [a' coefficient from Eq. (15)], in agreement with the results expressed in the literature [22,26,27].

As we did in Section 3.1 in Fig. 5, now to provide graphical proof of the goodness of the fitting polynomial in Eq. (15), in Fig. 8 we show the difference between the EWV calculated with the

Optics EXPRESS

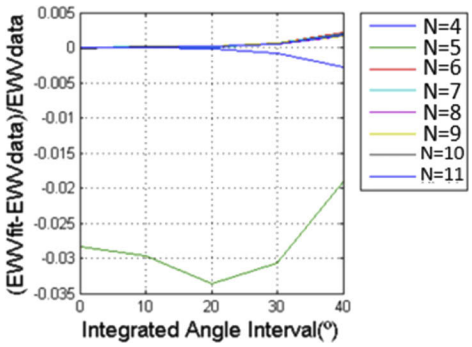

Fig. 8. Difference between the EWV calculated with the fitting polynomial [Eq. (15)] and the EWV data points, normalized by the data points.

fitted expression and the EWV data points in Fig. 7(b). This difference is normalized by the value of each of the EWV data points and represented as a function of the integrated angle interval $\Delta\theta$. The different curves correspond to different number of measurement analyzers, indicated in the legend as in Fig. 7(b). We remind that the polynomial fit in Eq. (15) did not consider the data corresponding to N = 5, since it follows a different pattern. We see that for the N≠5 the fit is excellent, with normalized differences smaller than ±0.005, with a slight increase at larger $\Delta\theta$. We note that in Fig. 5 the normalized differences were even smaller.

In the case of unrestricted orientations we have also obtained an analytical expression for the EWV as a function of N and $\Delta\theta$. Since now the orientations of the analyzers are not constrained to specific intervals, the EWV is smaller than in previous Section. However, the values are not very different what makes more interesting to apply the uniformly spaced angles since it is much easier to implement. We have also shown that the case for N = 5 follows a different pattern in terms of CN, EWV and optimal retardance. This is related with the fact that for N = 5, no distribution of the measurement states over the Poincaré sphere satisfies a spherical 2 design.

3.3. *Uniformly spaced angles for a quarter wavelength retarder and for a 128.1° retardance retarder*

Quarter wavelength retarders are easy to find in most laboratories. Therefore, we check if they offer a good performance when used in RRFP polarimeters when the integrated angle interval is considered. We focus on uniformly spaced angles, which is the practical working situation. In Figs. 9(a) and 9(b) we show the CN and the EWV as a function of $\Delta\theta$. When compared with Figs. 4(a) and 4(b) we see that the impact of noise in the polarimeter performance is more significant since the CN is higher than 3.5 even when $\Delta\theta = 0$, and EWV also becomes clearly larger. However, if the number of analyzers is increased, then the EWV diminishes into a practical value.

It is interesting to see the analyzers represented in the Poincaré sphere [Figs. 10(a) and 10(b)] for various integration angle intervals as we did previously in Fig. 6. In the present case, the degree of coverage of the Poincaré sphere is clearly smaller than in Fig. 6 even for $\Delta\theta = 0$. Thus, the obtained basis of analyzers encloses smaller volumes than those in Fig. 6, this leading to worse results for CN and EWV. Once again we see that the analyzers get into the volume of the Poincaré sphere when $\Delta\theta$ increases, thus the analyzers vectors become more depolarized with this parameter.

An interesting point to be addressed is if there is a fixed retardance value which might be a good choice for a retarder to be used along a wide range of possible $\Delta\theta$ values. We have seen that the quarter wavelength retarder, even being nowadays used in a number of RRFP implementations, is

Optics EXPRESS

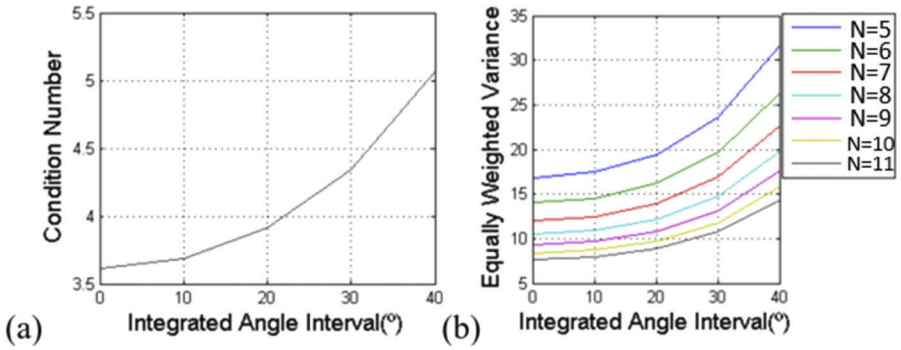

Fig. 9. Optimization results for the RRFP with uniformly spaced angles, and for a fixed retardance value of 90°. (a) CN and (b) EWV.

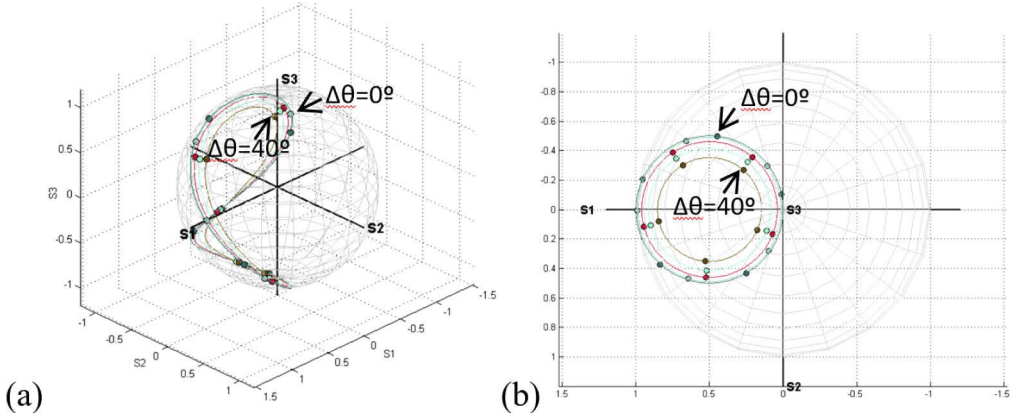

Fig. 10. Representation on the Poincaré sphere of the optimal analyzers for N = 5 when fixing the retardance value to 90°. The different trajectories are related with different integrated angle intervals: 0° (outer path), 10°, 20°, 30°, and 40° (inner path). In each of the trajectories the circles indicate the location of a particular set of measuring analyzers. (a) and (b) show different points of view of data in the Poincaré Sphere space.

not a very good choice. Now let us consider a fixed retardance value of 128.1°, i.e. the optimum value for the case $\Delta\theta = 0$ shown in Fig. 4(c) when uniformly spaced angle is considered. In Figs. 11(a) and 11(b) we show the results for CN and EWV as a function of $\Delta\theta$. We see that the values obtained are very similar to the ones obtained in Figs. 4(a) and 4(b). The values for CN are now a bit higher (worse polarimeters), but in the EWV we see that they are similar. This is important since a fixed retardance can be used regardless the average integration angle we need to apply.

In practical terms, when constructing a RRFP, the retarder has a fixed value which cannot be tuned to the specific integration angle interval $\Delta\theta$ associated with the RRFP measurement system. From the results in this Section for uniformly spaced angles, a fixed retardance value of 128.1° is an excellent election. Since this is not a standard retardance value for commercially available retarders, we have also shown the results with the easily available quarter wavelength retarders. They should not be the first choice since the CN and EWV are clearly higher. However, if the integration angle interval is less than 20° and the number of polarization analyzers is N ≥ 9, the EWV is smaller than 10: similar to the EWV for N = 5 for uniformly spaced angles [Fig. 4(b)] and for N = 4 for unrestricted orientations [Fig. 7(b)].

Optics EXPRESS

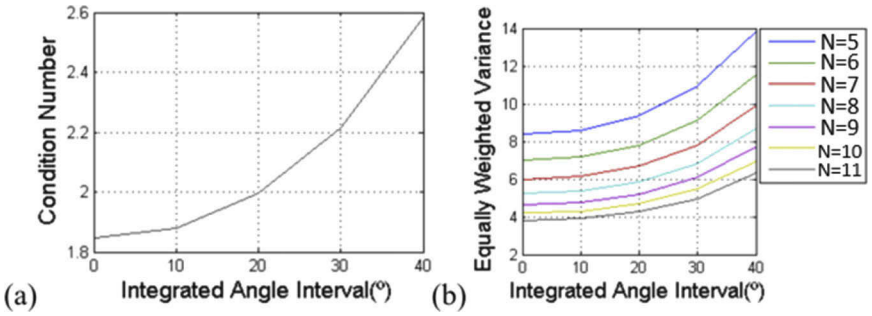

Fig. 11. Optimization results for the RRFP with uniformly spaced angles, and for a fixed retardance value of 128.1°. (a) CN and (b) EWV.

3.4. *Uniformly spaced angles for a non-achromatic zero order retarder with a retardance of 128.1 ° for 555 nm*

In the previous sections we have always considered that the illumination was monochromatic or that the retarder was achromatic, so that the chromatic dispersion of the retardance was not taken into account. Now we will consider the case of polychromatic illumination and a non-achromatic zero order retarder, which is a common situation. Let us consider that the retarder has a retardance of 128.1° at the wavelength 555 nm, which is in the center of the visible range. We want to know the performance when other wavelengths in the visible are used. To this goal we consider the two extreme cases, i.e. illuminating with a red wavelength and with a blue wavelength. The dependency of retardance Γ with wavelength for a zero order retarder is given by,

$$\Gamma(\lambda) = (2\pi/\lambda)\Delta n(\lambda)e \tag{16}$$

where λ is the illumination wavelength, e is the thickness of the retarder and Δn is the birefringence, which varies with the wavelength according to the dispersion function of the material composing the retarder. As a first approximation we consider Δn as a constant, since its variation is usually small compared with the effect of the parameter λ in Γ.

In Figs. 12(a) and 12(b) we show respectively the results of CN and average DOP, both for illumination with 555 nm and with 625 nm. Results for CN at 555 nm are the same as in Fig. 11 since the retardance is the same 128.1°. For 625 nm we see that CN is larger but still acceptable. The same happens with EWN, not represented here. The average DOP in Fig. 12(b) is larger in the case of 625 nm, since its retardance according to Eq. (16) is smaller than for 555 nm. The retardance at 625 nm is about 114°.

In Figs. 13(a) and 13(b) we show the same collection of results as in Fig. 12 but now instead of the red wavelength, we use the blue one (470 nm). As before CN gets higher (worse polarimeters) for the 470 nm when compared with 555 nm, as the system is not optimized for blue. However, the values are still good enough to be practical. For example, the CN is about 3 for 470 nm. The average DOP in Fig. 13(b) is now smaller in the case of 470 nm, since its retardance according to Eq. (16) is larger than for 555 nm, with a value of retardance about 151°.

In Figs. 14(a) and 14(b) we provide a geometrical visualization on the Poincaré sphere for the case with 11 analyzers, i.e. N = 11, and for various $\Delta\theta$ values from 0° to 40°. In Fig. 14(a) we combine the curves for 555 nm and for 625 nm. We see two differentiated groups of curves, where the ones closer to the poles are for 625 nm. In Fig. 14(b) we show the curves for 555 nm and 470 nm. Now the group of curves for 470 nm are further away from the poles. When retardance gets closer to 90°, the trajectories are closer to the poles, as in the red case, and the opposite happens for the blue. Volumes enclosed by different curves, are in agreement with data in Fig. 13.

Optics EXPRESS

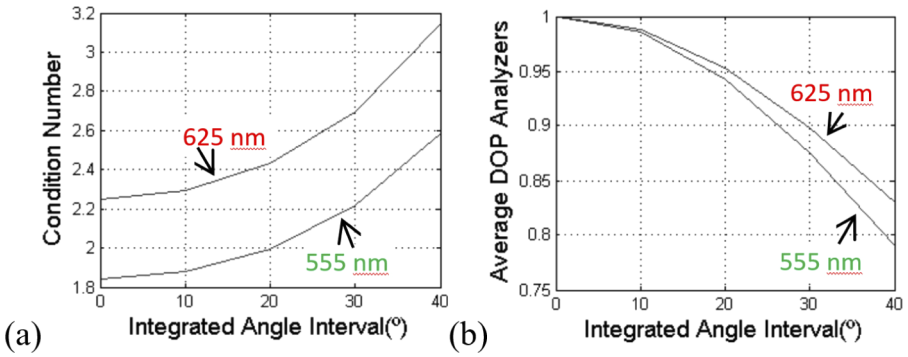

Fig. 12. Non-achromatic zero order retarder with fixed retardance value of 128.1° at 555 nm and 114° at 625 nm. Optimization results at 555 nm for the RRFP with uniformly spaced angles. (a) CN, and (b) average DOP.

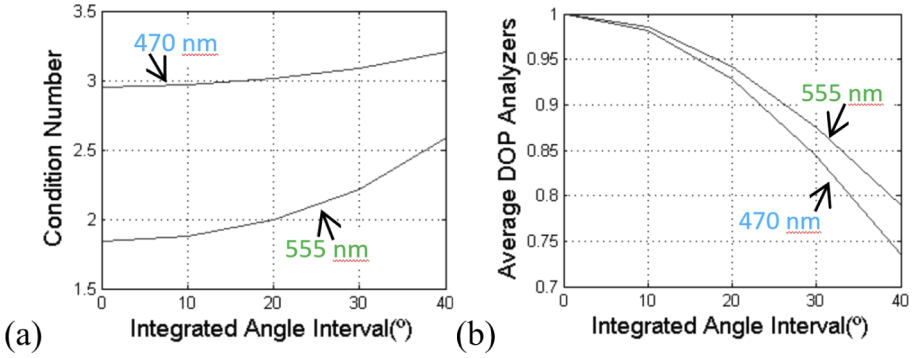

Fig. 13. Non-achromatic zero order retarder with fixed retardance value of 128.1° at 555 nm and 151° at 470 nm. Optimization results at 555 nm for the RRFP with uniformly spaced angles. (a) CN, and (b) average DOP.

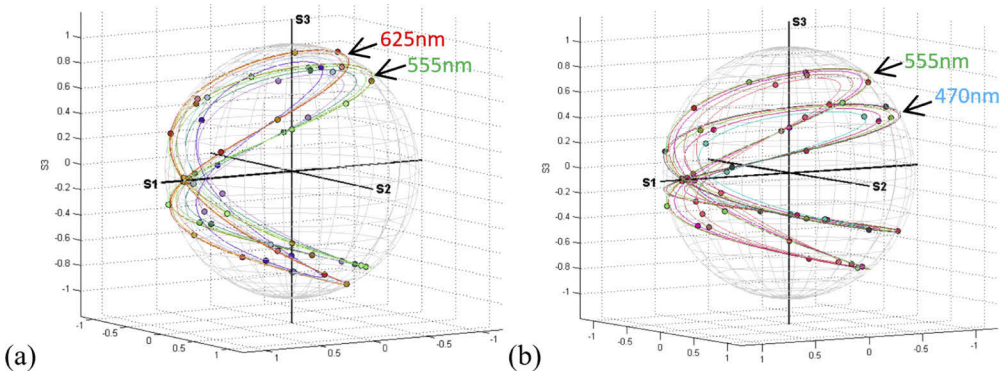

Fig. 14. Representation on the Poincaré sphere of the optimal analyzers at 555 nm for N = 11, for a RRFP with uniformly spaced angles and with a non-achromatic zero order retarder with fixed retardance values. The different trajectories are related with different integrated angle intervals: 0° (outer path), 10°, 20°, 30°, and 40° (inner path). In each of the trajectories the circles indicate the location of a particular set of measuring analyzers. (a) Fixed retardances of 128.1° at 555 nm and 114° at 625 nm. (b) Fixed retardances of 128.1° at 555 nm and 151° at 470 nm.

Optics EXPRESS

In the case of polychromatic illumination, when compared with the previous Section, we see that when constructing the RRFP it is preferable to use an achromatic retarder. The retardance of 128.1° is an excellent choice as shown in Section 3.3. In the case of non-achromatic zero order retarders in the present Section, we have shown that the noise amplification will depend on the wavelength. In our example, the retarder has a retardance of 128.1° for the 555 nm wavelength, and its noise amplification characteristics are clearly higher at the violet and red extremes of the visible spectrum.

4. Discussion about influence of noise sources and number of measurements

The results obtained for the CN and the EWV show the noise amplification due to the system of analyzers. Now we combine these results with the specific noise sources in the case of AWGN, which were presented in Section 2.2. They are the dark intensity noise and the read-out noise. Let us consider two different situations depending on the amount of light available for each of the measurements. For the forthcoming discussion we consider Eq. (12) to describe the EWV, and from this relation, we can define a global metric, the added variance v_{sum}, which considers the variances for the 4 Stokes vector components,

$$v_{sum} = \sum_{j=0}^{3} v_j = EWV(\varphi, \theta_k; \Delta\theta, N)\, u, \tag{17}$$

where u is the intensity noise (intensity variance), presented in Eq. (11) and Eq. (12), and where we show explicitly the dependencies of the EWV. In the results presented in previous Sections we have shown the optimal values for EWV for different values of integration angle intervals $\Delta\theta$ and number of analyzers N, where the retardance φ and the orientations θ_k for each of the N analyzers were the subject of optimization. What we obtained is that the optimal EWV decreases with the increase of N and with the decrease of $\Delta\theta$. We obtained analytical fitting expressions both in the case of uniformly spaced angles, Eq. (14), and for unrestricted orientations, Eq. (15). In the following we restrict our attention to the more practical case of uniformly spaced angles.

The SNR for the detection of each of the 4 Stokes components is given by $\langle S_i \rangle / \sqrt{v_i}$, where the subindex i denotes the Stokes component, and $\langle . \rangle$ indicates the average for an ensemble of Stokes vector estimates. We note that each of the estimates is calculated using Eq. (9) from the set of N intensity measurements given by the N polarization analyzers. When we consider the intensity measurements affected by AWGN with a zero mean, which is usually the case [27,28], then the average of the estimates $\langle S_i \rangle$ is unbiased and is a good estimator of the true value for the Stokes vector components. To be able to use the results obtained for the EWV in previous Sections we will adopt an alternative definition for the SNR,

$$SNR_{S_i} = \langle S_i \rangle / \sqrt{v_{sum}}, \tag{18}$$

First, let us consider that the N measurements can be taken with the same fix amount of light independently of the number N of analyzers and the integration angle interval. Introducing the added variance v_{sum} given in Eq. (17) into Eq. (18), we obtain,

$$SNR_{fix} = \frac{\langle S_i \rangle}{\sqrt{EWV(\varphi, \theta_k; \Delta\theta, N)\, u}}, \tag{19}$$

Then, better estimation of the Stokes vector is obtained when the added variance is smaller. Dark intensity noise, as shown in Eq. (13), depends on the integration time Δt: $u_{dark} = \langle I_{dark} \rangle \Delta t$. We are interested in relating it with the integration angle interval, which is the magnitude analyzed in the figures of the paper. The integration angle interval $\Delta\theta$ is related with the integration time of the sensor Δt and the angular frequency of rotation w_{ret} of the retarder $\Delta\theta = w_{ret}\Delta t$,

Optics EXPRESS

then $u_{dark} = \langle I_{dark} \rangle \, \Delta\theta / \, w_{ret}$. We obtain that the shorter $\Delta\theta$, the smaller the variance u_{dark} in the intensity. If we combine this with Eq. (14) and (19), then

$$SNR_{fix,dark} = \langle S_i \rangle \Big/ \sqrt{\frac{(a+b\,\Delta\theta^2+c\,\Delta\theta^4+d\,\Delta\theta^6+e\,\Delta\theta^8)}{N} \frac{\langle I_{dark} \rangle \Delta\theta}{w_{ret}}}, \tag{20}$$

and now we eliminate the parameters constant with the integration angle interval and the number of measurements, so that the SNR is proportional to

$$SNR_{fix,dark} \propto \frac{\sqrt{N}}{\sqrt{(a + b\,\Delta\theta^2 + c\,\Delta\theta^4 + d\,\Delta\theta^6 + e\,\Delta\theta^8)\Delta\theta}}, \tag{21}$$

This means that the SNR increases for larger number N of analyzers and for shorter $\Delta\theta$. In the case of read-out noise, the variance is a constant number per frame, i.e. it does not depend on the integration angle interval. In this case, apart from constant factors, Eq. (19) produces the following proportional SNR expression,

$$SNR_{fix,read} \propto \frac{\sqrt{N}}{\sqrt{(a + b\,\Delta\theta^2 + c\,\Delta\theta^4 + d\,\Delta\theta^6 + e\,\Delta\theta^8)}}, \tag{22}$$

and the SNR increases for larger number N of analyzers and for shorter $\Delta\theta$ as in Eq. (21) but with different dependence on $\Delta\theta$.

We show in Figs. 15(a) and 15(b) the results, normalized to one, produced respectively with Eqs. (21) and (22). In Fig. 15(a), for dark shot noise, we show the region between 0 and 4 integrated angle interval, since in this the part is where the best SNR is obtained: we see that the best value is produced for N = 11 and $\Delta\theta = 0$, as expected. In Fig. 15(b) we show a black region where data accomplish the relation $\Delta\theta > \pi / N$, this black area corresponding to integration angle intervals larger than the separation between consecutive measurements. As stated in previous Sections, this is not allowed by construction, to avoid angular overlap, so this black area is not considered for the study. In turn, we see that within the allowed area, the best results occur for N = 11 and $\Delta\theta = 0$, as in Fig. 15(a) but with larger tolerances.

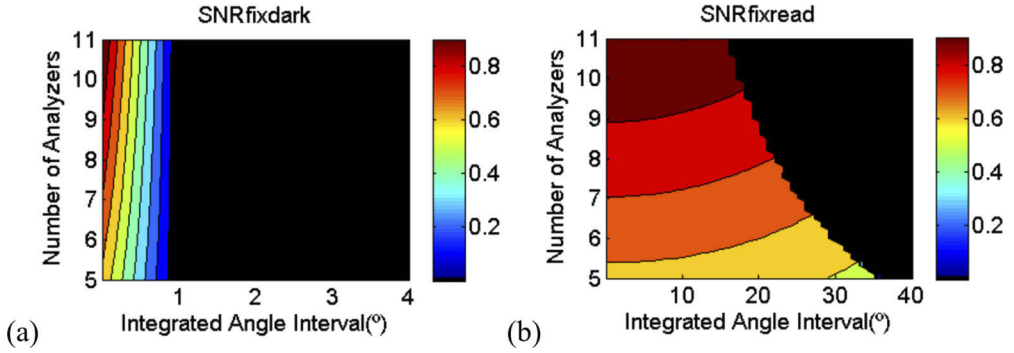

Fig. 15. SNR results for the RRFP with uniformly spaced angles and for a fix amount of photons per measurement for, (a) dark shot noise, and (b) read-out noise, obtained as a function of the number of analyzers N and the integrated angle interval $\Delta\theta$.

Let us now consider the case when the amount of photons is limited [27], i.e. a constant amount of photons is shared by the N measurements during half a rotation of the retarder. This can be called the "photon-starved" scenario [26]. If we call $\bar{S}$ to the Stokes vector being measured expressed in the number of photons incident during half a rotation, then the amount of photons

Optics EXPRESS

collected in one measurement are proportional to the integration angle interval, that is $\vec{S}\Delta\theta \Big/ \pi$. Therefore, the intensity vector in Eq. (8) becomes,

$$\vec{I} = \frac{\Delta\theta}{\pi} W\vec{S}. \tag{23}$$

The estimated Stokes vector in Eq. (9) now is given by,

$$\vec{S} = \frac{\pi}{\Delta\theta} W^{+}\vec{I}, \tag{24}$$

and the added variance $v_{sum,lim}$ in the photon limited case becomes,

$$v_{sum,lim} = \left(\frac{\pi}{\Delta\theta}\right)^2 EWV(\varphi, \theta_k; \Delta\theta, N)\, u, \tag{25}$$

which can be expressed as a function of the added variance v_{sum} in Eq. (17),

$$v_{sum,lim} = \left(\frac{\pi}{\Delta\theta}\right)^2 v_{sum}. \tag{26}$$

The signal-to-noise ratio for this case of limited amount of photons is now given by,

$$SNR_{lim} = \frac{\langle S_i \rangle}{\sqrt{v_{sum,lim}}}, \tag{27}$$

which can be rewritten using Eqs. (17) and (26),

$$SNR_{lim} = \frac{\Delta\theta}{\pi} \frac{\langle S_i \rangle}{\sqrt{EWV(\varphi, \theta_k; \Delta\theta, N)\, u}}, \tag{28}$$

If we now consider the relation $u_{dark} = \langle I_{dark} \rangle \Delta\theta / w_{ret}$ for the dark intensity noise together with Eq. (14), and eliminate the constant parameters, then we obtain,

$$SNR_{lim,dark} \propto \frac{\sqrt{N\Delta\theta}}{\sqrt{(a + b\,\Delta\theta^2 + c\,\Delta\theta^4 + d\,\Delta\theta^6 + e\,\Delta\theta^8)}}. \tag{29}$$

In the case of read-out noise, it is a constant value per frame and it does not depend on the integration angle interval, thus the SNR becomes,

$$SNR_{lim,read} \propto \frac{\sqrt{N}\Delta\theta}{\sqrt{(a + b\,\Delta\theta^2 + c\,\Delta\theta^4 + d\,\Delta\theta^6 + e\,\Delta\theta^8)}}. \tag{30}$$

To analyse Eqs. (29) and (30) we proceed with a graphical representation as a function of $\Delta\theta$ and N to find the points at which SNR is maximized. In Figs. 16(a) and 16(b) we show the results, normalized to one, respectively for dark shot noise and for read-out noise. As in Fig. 15(b), we show in black the region where $\Delta\theta$ becomes larger than the maximum integration angle interval as a function of the number of measurements, given by $\Delta\theta_M = \pi / N$. We see that for dark shot noise, Fig. 16(a), better SNR values are obtained with the increase in N and $\Delta\theta$. In the case of read-out noise, Fig. 16(b), better results correspond to larger $\Delta\theta$ and for N = 5.

In the analysis of the signal-to-noise ratio for AWGN we have combined the noise amplification characteristics of the system of analyzers, through the EWV, and the specifications of the particular intensity noise sources, through the uncertainty dependencies for the dark current noise and the read-out noise. Results in Figs. 15 and 16 show respectively for the case of fix and limited amount of photons per measurement, which are the best configurations of N and $\Delta\theta$. In the case of fix amount, both for dark current and read-out noise, it is recommended the higher number of analyzers and smaller integration angle interval possible. In the case of limited amount, larger integration angle intervals are preferable, and the number of polarization analyzers must be high for dark current noise and equal to N = 5 for read-out noise.

Optics EXPRESS

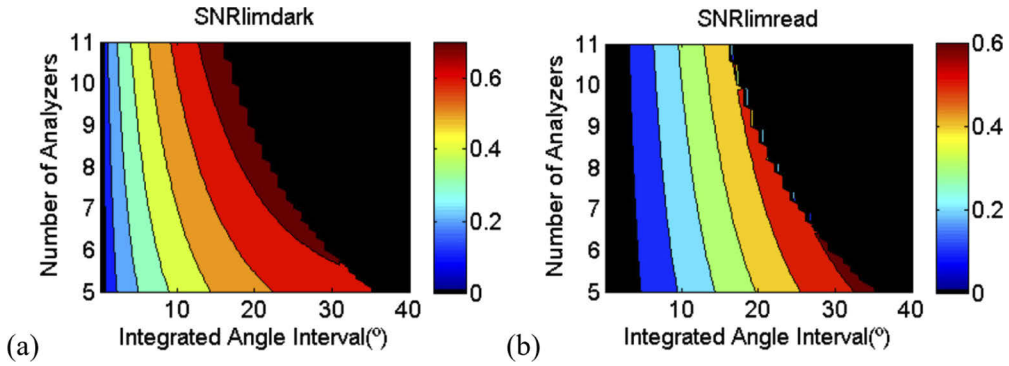

Fig. 16. SNR results for the RRFP with uniformly spaced angles and for a limited amount of photons, for half a rotation of the retarder, and when the photons are shared by the N measurements, for (a) dark shot noise, and (b) read-out noise, obtained as a function of the number of analyzers N and the integrated angle interval $\Delta\theta$.

5. Conclusions

We have studied the optimum operating conditions for a RRFP where the measurements are not quasi-instantaneous, which is a common situation, to certain extent, in real RRFP implementations. We have obtained the optimum retardance and retarder orientations as a function of the integrated angle interval $\Delta\theta$ and the number N of polarization analyzers. Two different analyzers configurations have been studied in this work: for uniformly spaced retarder angles and when measurements are taken at optimum angles (non-uniformly spaced angles or unrestricted orientations). We have also considered the case of polychromatic illumination. We have discussed the best measurement conditions in terms of the SNR, when the light sensor noise sources are AWGN and depending if there is a fix or a limited amount of photons per measurement.

One important result is that, both for uniformly spaced angles and for unrestricted orientations, we have obtained the analytical expressions for the EWV as a function of N and $\Delta\theta$. This includes as a particular result the case for fully polarized analyzers, which is the usual situation considered in the literature. We find that the EWV is just slightly smaller for the case of unrestricted orientations: as a result, it is more interesting for the RRFP to operate with uniformly spaced angles since it is much easier to implement in practice.

We have also obtained that the optimum retardance increases with $\Delta\theta$ and is independent of the number N of analyzers, the only exception being the case for $N = 5$ for unrestricted orientations. In practical terms, when constructing a RRFP, the retarder has a fix retardance value regardless of the $\Delta\theta$ value at which the RRFP operates. We have shown that for uniformly spaced angles, a fix retardance value of 128.1° is an excellent election. The quarter wavelength retarder, much more easily available, produces a much higher noise amplification and only if $\Delta\theta < 20$ and the number of polarization analyzers is $N \geq 9$, its EWV achieves a reasonable value. In the case of polychromatic illumination, when using a non-achromatic zero order retarder the noise amplification depends on the wavelength. For the visible spectrum situation evaluated in the paper, where we consider the retarder to have a retardance of 128.1° in the center of the spectrum (555 nm), its noise amplification characteristics are clearly higher at the violet and red extremes of the visible spectrum, but it is still within practical limits.

The discussion for the SNR has been done through analytical expressions, for the practical case of uniformly spaced angles and AWGN. Results show respectively for the case of fix and limited amount of photons per measurement, which are the best configurations of N and $\Delta\theta$. In the case of fix amount, both for dark current and read-out noise, it is recommended the higher number of

Optics EXPRESS

analyzers and smaller integration angle interval possible. In the case of limited amount, larger integration angle intervals are preferable, and the number of polarization analyzers must be high for dark current noise and equal to N = 5 for read-out noise.

Funding

Ministerio de Economía y Competitividad (Fondos Feder, RTI2018-097107-B-C31); Agència de Gestió d'Ajuts Universitaris i de Recerca (SGR 2017-00150).

Disclosures

The authors declare no conflicts of interest related to this article.

References

1. M. Anastasiadou, A. De Martino, D. Clement, F. Liège, B. Laude-Boulesteix, N. Quang, J. Dreyfuss, B. Huynh, A. Nazac, L. Schwartz, and H. Cohen, "Polarimetric imaging for the diagnosis of cervical cancer," Phys. Status Solidi **5**(5), 1423–1426 (2008).
2. K. M. Twietmeyer, R. A. Chipman, A. E. Elsner, Y. Zhao, and D. VanNasdale, "Mueller matrix retinal imager with optimized polarization conditions," Opt. Express **16**(26), 21339 (2008).
3. A. Van Eeckhout, A. Lizana, E. Garcia-Caurel, J. J. Gil, A. Sansa, C. Rodríguez, I. Estévez, E. González, J. C. Escalera, I. Moreno, and J. Campos, "Polarimetric imaging of biological tissues based on the indices of polarimetric purity," J. Biophotonics **11**(4), e201700189 (2018).
4. L. J. November and L. M. Wilkins, "Liquid Crystal Polarimeter for solid state imaging of solar vector magnetic fields," in D. H. Goldstein and D. B. Chenault, eds. (International Society for Optics and Photonics, 1994), Vol. 2265, p. 210.
5. J. Hough, "Polarimetry: a powerful diagnostic tool in astronomy," Astron. Geophys. **47**(3), 3.31–3.35 (2006).
6. A. Márquez, I. Moreno, C. Iemmi, A. Lizana, J. Campos, and M. J. Yzuel, "Mueller-Stokes characterization and optimization of a liquid crystal on silicon display showing depolarization," Opt. Express **16**(3), 1669–1685 (2008).
7. S. Firdous and M. Ikram, "Stokes Polarimetry for the Characterization of Bio-Materials using Liquid Crystal Variable Retarders," in *Therapeutic Laser Applications and Laser-Tissue Interactions III*, A. Vogel, ed., Vol. 6632 of Proceedings of SPIE-OSA Biomedical Optics (Optical Society of America, 2007), paper 6632_14.
8. E. Garcia-Caurel, R. Ossikovski, M. Foldyna, A. Pierangelo, B. Drévillon, and A. De Martino, "Advanced Mueller Ellipsometry Instrumentation and Data Analysis," in M. Losurdo and K. Hingerls, eds., (Springer-Varlag, 2013).
9. G. E. Jellison, "Four-channel polarimeter for time-resolved ellipsometry," Opt. Lett. **12**(10), 766–768 (1987).
10. J. S. Tyo, D. L. Goldstein, D. B. Chenault, and J. A. Shaw, "Review of passive imaging polarimetry for remote sensing applications," Appl. Opt. **45**(22), 5453–5469 (2006).
11. D. S. Sabatke, M. R. Descour, E. L. Dereniak, W. C. Sweatt, S. A. Kemme, and G. S. Phipps, "Optimization of retardance for a complete Stokes polarimeter," Opt. Lett. **25**(11), 802–804 (2000).
12. A. Peinado, A. Lizana, J. Vidal, C. Iemmi, and J. Campos, "Optimization and performance criteria of a Stokes polarimeter based on two variable retarders," Opt. Express **18**(10), 9815–9830 (2010).
13. A. Van Eeckhout, E. Garcia-Caurel, T. Garnatje, M. Durfort, J. C. Escalera, J. Vidal, J. J. Gil, J. Campos, and A. Lizana, "Depolarizing metrics for plant samples imaging," PLoS One **14**(3), e0213909 (2019).
14. S. J. Matcher, M. Cope, and D. T. Delpy, "In vivo measurements of the wavelength dependence of tissue-scattering coefficients between 760 and 900 nm measured with time-resolved spectroscopy," Appl. Opt. **36**(1), 386 (1997).
15. S. Carvalho, N. Gueiral, E. Nogueira, R. Henrique, L. Oliveira, and V. V. Tuchin, "Wavelength dependence of the refractive index of human colorectal tissues: comparison between healthy mucosa and cancer," J. Biomed. Photonics Eng. **2**(4), 040307 (2016).
16. J. Soni, H. Purwar, H. Lakhotia, S. Chandel, C. Banerjee, U. Kumar, and N. Ghosh, "Quantitative fluorescence and elastic scattering tissue polarimetry using an Eigenvalue calibrated spectroscopic Mueller matrix system," Opt. Express **21**(13), 15475–15489 (2013).
17. R. A. Chipman, "Polarimetry," in *Handbook of Optics*, (McGraw-Hill, 1995), Chap. 22.
18. https://www.thorlabs.com/newgrouppage9.cfm?objectgroup_id=1564 (visited 30th October 2019)
19. J. J. Gil and R. Ossikovski, "Polarized Light and the Mueller Matrix Approach," in *Series in Optics and Optoelectronics*, (CRC, Taylor&Francis Group, 2016).
20. P. Taylor, "Theory and Applications of Numerical Analysis," (Academic, 1974).
21. E. Chironi and C. Iemmi, "Bounding the relative errors associated with a complete Stokes polarimeter," J. Opt. Soc. Am. A **31**(1), 75–80 (2014).
22. M. R. Foreman and F. Goudail, "On the equivalence of optimization metrics in Stokes polarimetry," Opt. Eng. **58**(08), 1 (2019).
23. http://www.emva.org/standards-technology/emva-1288/ (visited 30th October 2019)
24. M. R. Foreman, A. Favaro, and A. Aiello, "Optimal Frames for Polarization State Reconstruction," Phys. Rev. Lett. **115**(26), 263901 (2015).

Optics EXPRESS

25. A. Lizana, J. Campos, A. Van Eeckhout, and A. Marquez, "Misalignment error analysis in polychromatic division of focal plane Stokes polarimeters," OSA Continuum **2**(5), 1565–1575 (2019).
26. F. Goudail, "Equalized estimation of Stokes parameters in the presence of Poisson noise for any number of polarization analysis states," Opt. Lett. **41**(24), 5772–5775 (2016).
27. F. Goudail and A. Bénière, "Estimation precision of the degree of linear polarization and of the angle of polarization in the presence of different sources of noise," Appl. Opt. **49**(4), 683–693 (2010).
28. J. Dai, F. Goudail, M. Boffety, and J. Gao, "Estimation precision of full polarimetric parameters in the presence of additive and Poisson noise," Opt. Express **26**(26), 34081–34093 (2018).